J Biol Inorg Chem
DOI 10.1007/s00775-015-1251-9

ORIGINAL PAPER

Structural characterization of metal binding to a cold-adapted frataxin

Martín E. Noguera[1] · Ernesto A. Roman[1] · Juan B. Rigal[1] · Alexandra Cousido-Siah[2] · André Mitschler[2] · Alberto Podjarny[2] · Javier Santos[1]

Received: 4 September 2014 / Accepted: 2 March 2015

Abstract Frataxin is an evolutionary conserved protein that participates in iron metabolism. Deficiency of this small protein in humans causes a severe neurodegenerative disease known as Friedreich's ataxia. A number of studies indicate that frataxin binds iron and regulates Fe–S cluster biosynthesis. Previous structural studies showed that metal binding occurs mainly in a region of high density of negative charge. However, a comprehensive characterization of the binding sites is required to gain further insights into the mechanistic details of frataxin function. In this work, we have solved the X-ray crystal structures of a cold-adapted frataxin from a psychrophilic bacterium in the presence of cobalt or europium ions. We have identified a number of metal-binding sites, mainly solvent exposed, several of which had not been observed in previous studies on mesophilic homologues. No major structural changes were detected upon metal binding, although the structures exhibit significant changes in crystallographic *B*-factors. The analysis of these *B*-factors, in combination with crystal packing and RMSD among structures, suggests the existence of localized changes in the internal motions. Based on these results, we propose that bacterial frataxins possess binding sites of moderate affinity for a quick capture and transfer of iron to other proteins and for the regulation of Fe–S cluster biosynthesis, modulating interactions with partner proteins.

Keywords CyaY protein family · Iron binding · X-ray diffraction · Conformational dynamics · Extremophile

Introduction

Frataxin (FXN) is a highly conserved protein that plays an essential role in iron homeostasis [1]. Furthermore, it has been a focus of attention because its deficiency causes the neurodegenerative disease known as Friedreich's ataxia. Despite extensive research, the exact function of FXN remains elusive and several roles have been proposed, including an iron chaperone activity and the regulation of iron–sulfur (Fe–S) cluster assembly [2]. Notably, the effect of FXN in Fe–S cluster biosynthesis appears to differ between eukaryotes and prokaryotes [3]: in the former, in vitro experiments indicate that FXN promotes cysteine desulfurase activity and Fe–S cluster assembly, whereas in the latter, binding of FXN to the assembly complex inhibits Fe–S cluster synthesis. Accordingly, in vivo experiments have shown that frataxin knockdown in eukaryotes causes severe alterations in the levels of Fe–S cluster-containing enzymes [4], while knockdown in bacteria seems not to impede cell viability [5].

The native structure of FXN has already been solved by NMR and crystallography for human [1, 6], yeast [7, 8] and bacterial homologs [9–11]. It consists of a five-stranded antiparallel β-sheet, tightly packed against two parallel α-helices. Despite the differences in length of the N- and C-terminal regions, structures of FXN homologs are practically superimposable. One notable feature of the

An Interactive 3D Complement page in Proteopedia is available at: http://proteopedia.org/w/Journal:JBIC:30.

Electronic supplementary material The online version of this article (doi:10.1007/s00775-015-1251-9) contains supplementary material, which is available to authorized users.

✉ Javier Santos
javiersantosw@gmail.com

[1] Instituto de Química y Físico-Química Biológicas, Universidad de Buenos Aires, Junín 956, 1113AAD Buenos Aires, Argentina

[2] Department of Integrative Biology, IGBMC, CNRS, INSERM, Université de Strasbourg, Illkirch, France

Published online: 02 April 2015

FXN family of structures is the presence of a high density of acidic residues in the N-terminal, forming the so-called "acidic ridge" (helix α1, loop1 and strand β1). A large number of biophysical studies have identified this region as an iron-binding surface, involved in the biological function [10, 12–14]. Anaerobic isothermal titration calorimetry demonstrates that two Fe^{2+} atoms or six Fe^{3+} (upon Fe^{2+} oxidation by H_2O_2) are specifically bound per protein monomer for the bacterial homolog from *Escherichia coli* (called eFXN throughout this article) [15]. Noteworthy, eFXN interacts through its acidic ridge with a positively charged surface on the IscS protein, one of the main players of the Fe–S cluster assembly machinery, the same surface used by IscS to bind other negatively charged surfaces on protein partners, as demonstrated for ferredoxin [16]. Therefore, we hypothesize that some of the iron-binding sites on FXN might play a regulatory role modifying binding affinities and modulating IscS function.

To gain further insights on the metal-binding plasticity of frataxin, we have focused on the homolog protein from the psychrophilic bacterium *Psychromonas ingrahamii* [17], herein named pFXN. More importantly, the structure of the mesophilic homolog from *Escherichia coli* (eFXN) has been solved in the presence and absence of metal ions (Co^{2+} and Eu^{3+}), revealing no significant alteration in structure upon binding [18]. Although the structures of both homologs are highly similar, with only a slight difference in the length of loop1, there are a number of features that make pFXN a very attractive model to study stability–dynamics–function relationships. First, thermodynamic stability is highly pH dependent only in the psychrophilic variant, increasing from a very low stability at pH 8 (~1 kcal/mol) to ~6 kcal/mol at pH 6, with a concomitant variation in T_m from 55.0 to 33.1 °C, at pH 6.0 and pH 8.0, respectively [11]. Furthermore, the content and localization of some residues, which in principle may be important for iron-binding activity, such as histidines and the acidic residues of the "acidic ridge", also differ.

It is worthy of note that none of the FXN homologs studied so far exhibits a stability dependence on pH as large as observed for pFXN. The stability of the human FXN variant Hfra-(91–210) is near invariant between pH 6.0 and 9.0 [19] and similarly, the stability of eFXN shows no significant dependence on pH over the range 6.0–8.0 [20]. The yeast FXN shows a significant but smaller stability dependence on pH as judged by the change in T_m from thermal unfolding experiments, with T_m values of 39.9, 35.4 and 33.0 °C for pH values of 6.0, 7.0 and 8.0, respectively [20].

Remarkably, the range of variation in stability experienced by pFXN as pH changes captures the stability difference observed for the FXN homologs: in the lower limit, yeast FXN exhibits very low stability (~1.4 kcal/mol) [14], whereas human FXN exhibits the highest stability (8–9 kcal/mol) [21]. A deep understanding of stability modulation in the FXN fold is needed not only for the basic knowledge of its folding mechanism, but also to rationalize the impact of clinical mutations with possible applications in molecular medicine [19].

In this work, we have solved the structures of pFXN in complex with the transition metals Co^{2+} and Eu^{3+}, used as surrogates to probe iron-binding sites [18]. Experiments with Fe^{2+} require strictly anaerobic or reducing conditions that could potentially interfere with the binding assay. On the other hand, acidic conditions are necessary to inhibit Fe^{3+} precipitation. These render difficult-to-conduct X-ray experiments in the presence of iron. For these reasons, Co^{2+} is a commonly used mimetic for Fe^{2+} that allows to conduct experiments under aerobic conditions, whereas Eu^{3+} was previously used as a trivalent metal analog, as in the case of binding to eFXN. The obtained structures, together with the previously reported one, in the absence of transition metals (herein named "apo-pFXN") [11], have allowed us to investigate the geometry of binding sites and the effect of metal binding in the pFXN structure.

Materials and methods

Crystallization and data collection

The frataxin from *P. ingrahamii* (pFXN) was expressed, purified and crystallized as described in our previous article [11]. Briefly, crystals were obtained at 24 °C by the hanging drop method, and the drop was a 1:1 mix of protein (17 mg/ml in 20 mM Tris–HCl, 100 mM NaCl, pH 7.0) and reservoir solution (200 mM sodium acetate, 200 mM $MgCl_2$, 27.5 % polyethylene glycol 4000, pH 4.8). For soaking experiments, crystals of pFXN were incubated in the crystallization solution supplemented with 200 mM $CoCl_2$ or 200 mM $EuCl_3$, and incubated for 5 h. The X-ray diffraction data were collected at 100 K on the X06DA beamline at the Swiss Light Source (SLS) (Switzerland), using a Pilatus 2 M detector (Dectris Ltd., Baden, Switzerland). Prior to data collection, crystals were cryoprotected by soaking in 200 mM sodium acetate pH 4.7, 200 mM $MgCl_2$, 34 % polyethylene glycol 4000 and 5 % ethylene glycol and flash-cooled in liquid nitrogen. The diffraction data were processed using the HKL2000 suite of programs [22]. Five percent of the measured reflections were flagged for cross-validation [23]. Data collection and processing statistics are given in Table 1.

Structure solution, refinement, and validation

The crystal structures were solved by molecular replacement (MR) using the coordinates of pFXN in the "apo

Table 1 Data collection and refinement statistics

	Co^{2+} derivative	Eu^{3+} derivative
Data collection		
Wavelength (Å)	0.91907	0.91907
Space group	P 1 21 1	P 1 21 1
Unit cell parameters		
a (Å)	39.89	39.89
b (Å)	50.56	49.99
c (Å)	46.31	46.58
α (°)	90.00	90.00
β (°)	90.77	90.43
γ (°)	90.00	90.00
Resolution limits (Å)	30.43–1.49 (1.55–1.49)	31.15–1.80 (1.92–1.80)
R_{sym} (%)	4.5 (25.3)	5.0 (33.6)
$I/\sigma(I)$	20.6 (3.34)	16.5 (3.48)
Completeness (%)	98.0 (92.0)	96.8 (91.7)
Redundancy	3.2 (2.4)	3.0 (2.9)
V_M ($Å^3$ Da^{-1})	1.90	1.89
Solvent content (%)	35.2	34.9
No. molecules in ASU	2	2
Refinement		
Resolution limits (Å)	30.425–1.494	31.147–1.803
Number of reflections	29,167	16,054
R_{work}/R_{free} (%)	18.39/21.06	21.35/26.02
No. protein atoms	1737	1718
No. water molecules	145	40
Deviations from ideal geometries		
Bond length (Å)	0.019	0.010
Bond angles (°)	1.781	1.235
Ramachandran plot		
Most favored (%)	99.5	98.5
Allowed (%)	0.5	1.5

Data correspond to merged F^+ and F^-. Values in parentheses refer to the highest resolution shell

form" Protein Data Bank (PDB) entry 4HS5 [11]. In the case of the cobalt-soaked crystal, MR was performed using Phaser [24] as implemented in the Phenix suite [25], whereas in the case of europium-soaked crystal, MR was obtained using Phaser, but implemented in the MrBump program [26] from the CCP4 suite [27]. Refinement was carried out using REFMAC5 [28] interspersed with manual model building using Coot [29]. Metal atoms were identified from anomalous difference Fourier maps. *B*-factors of protein atoms were treated using TLS refinement (one group per chain). Final refinement was carried out using Phenix. The stereochemical quality of the model was checked using the Molprobity server [30]. The atomic coordinates and structure factors have been deposited in the PDB (entries 4LP1 and 4LK8).

Structural analysis

Protein–metal contacts and intermolecular contacts including symmetry-related molecules were calculated with the CONTACT program in the CCP4 suite. Normalized temperature factors (B') were calculated with the formula $B' = (B - \langle B \rangle)/\sigma(B)$, where B is the B-factor (the isotropic equivalent when the protein was solved with TLS refinement), $\langle B \rangle$ and $\sigma(B)$ are the mean and the standard deviation of B-factors, respectively. The NOC program (http://noch.sourceforge.net/) was used for structure superposition and root mean square deviation (RMSD) calculation. Glu105, which is the last residue, was omitted in all contact calculations because it is not visible in the Eu derivative structure.

Model validation from statistical analysis of electron density maps, using the RSZD+, RSZD− and RSZO scores, was performed using the EDSTATS program in the CCP4 suite [31]. We used the computed difference Fourier and Fourier maps from the last run of refinement for apo-pFXN and its metal derivatives.

Iron-binding experiments

A quantitative characterization of iron-binding stoichiometry and affinity was carried out using fluorescence quenching experiments. Steady-state fluorescence measurements were performed in an Aminco Bowman Series 2 spectrofluorometer, equipped with a thermostated cell holder connected to a circulating water bath set at 25 °C. Emission spectra were collected from 300–450 nm, using excitation wavelength of 295 nm, with spectral slit-widths set to 4 nm for both monochromators. A sample of 2 ml of a 6 μM solution of pFXN in 20 mM sodium acetate, 100 mM NaCl, pH 4.8 was placed in a stirred, 1-cm path-length cuvette, and a 2.5 mM $FeCl_3$ solution (prepared in 10 mM HCl) was added in 2 μl increments, followed by 3 min of equilibration. No significant shifts in pH were measured upon completion of the experiment. An equivalent UV–visible titration was carried out to correct for the inner filter effect, and the corrected fluorescence intensity at 330 nm (F_{corr}) was determined from the observed intensity (F_{obs}) using the equation [32]:

$$F_{corr} = F_{obs} \times 10^{(A_{295}+A_{330})/2}.$$

The stoichiometry (p) and apparent dissociation constant (K_D) were obtained from a non-linear regression procedure, using a model of equivalent and independent binding sites to fit to the data [33]. First to all, the F_{corr} was used to calculate the fractional signal change (Y):

$$Y = (y_0 - y_f)/(y_b - y_f),$$

where y_0 is the F_{corr} at a given iron concentration, y_b and y_f are the F_{corr} when the binding sites are fully occupied and unoccupied, respectively. Fractional signal change was related to the iron concentration through the equation:

$$Y = \frac{K_D + L_t + p \cdot P_t - \sqrt{(K_D + L_t + p \cdot P_t)^2 - 4p \cdot P_t \cdot L_t}}{2p \cdot P_t},$$

where L_t and P_t are the total ligand and protein concentrations, respectively.

Hydrodynamic behavior

The aggregation state was investigated by static light scattering using a miniDawn instrument (Wyatt Technology) coupled to a size-exclusion Superose-12 column (GE Healthcare). The elution buffer was 20 mM sodium acetate, 100 mM NaCl, pH 4.8. Protein concentration was 790 μM and the experiment was carried out at room temperature (~25 °C) and at a 0.4 ml/min flow rate. Data analysis was performed using the Astra 6.0 software (Wyatt Technology).

Results

Overall structure and metal-binding sites

Crystal structures of pFXN in complex with the transition metals Co^{2+} and Eu^{3+} belong to the monoclinic space group $P2_1$ in a similar way to apo-pFXN, and cell content analysis also indicates the presence of two protein molecules per asymmetric unit (Fig. 1). Even when apo-pFXN has shown to be mainly monomeric in solution, a significant fraction (30 % at pH 4.8) behaves as a dimer, as evaluated using light scattering at high protein concentration (790 μM, Fig. 2). A similar behavior was observed at pH 7.0 (Figure S1). However, the protein is monomeric at low concentration (30 μM, Figure S2). These results suggest that dimerization is unspecific or governed by a low association constant, and it is only manifested at high protein concentrations, as used for light scattering measurements. Accordingly, analysis of the crystal assembly using the PISA server [34] scores the interface found in the asymmetric unit as unstable. All the residues could be located in the electron density maps, with the exception of the last C-terminal residue (Glu105) of the Eu^{3+} derivative, possibly due to disorder.

Initial anomalous difference maps, as well as refined single and double difference maps (Fc–Fo and 2Fc–Fo), showed several strong peaks that were assigned to metal

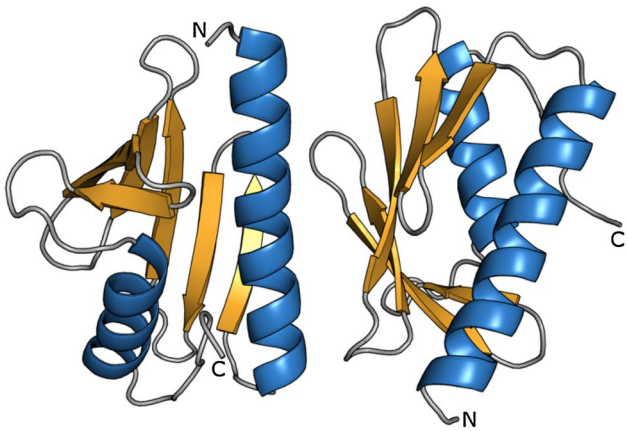

Fig. 1 The asymmetric unit of pFXN crystals. The same dimeric assembly is found in structures of apo-pFXN and its metal derivatives, and it is depicted here as ribbon representation, with N- and C-terminal labeled

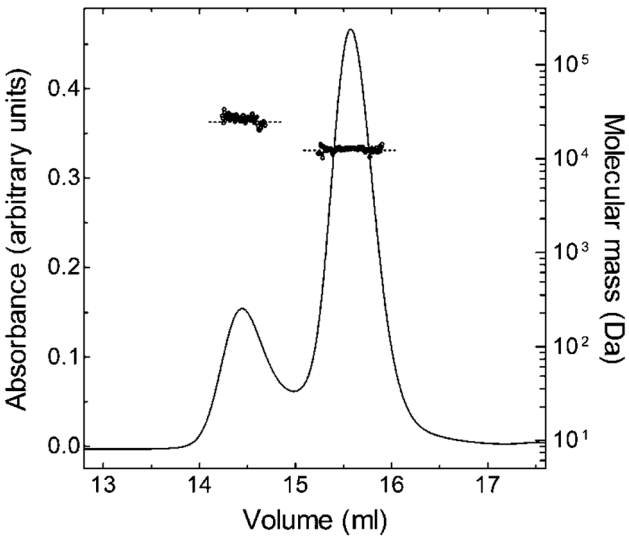

Fig. 2 Hydrodynamic properties of pFXN. The elution profile of pFXN from a size-exclusion Superose 12 column is shown. The elution was monitored using absorbance at 280 nm (*solid line*) and multi-angle light scattering (MALS, *circles*). The molecular weight (MW) of pFXN was determined using MALS, and compared to the MW of monomeric or dimeric pFXN calculated from the amino acid composition (indicated as *horizontal bars*). Elution buffer was 20 mM sodium acetate, 100 mM NaCl, pH 4.8 and the experiment was carried out at 25 °C. Protein concentration was 790 μM

ions (Table 2). The occupancies of metals were refined to be consistent with the surrounding atoms' *B*-factors. The low occupancy and alternative positions of some of these metals are indicative of certain degree of crystal static disorder, suggesting variability in the mode of binding at these sites. Moreover, metal localization differs between monomers of the asymmetric unit. Besides the intrinsic affinity of binding sites, it should be noted that

Table 2 Metal–pFXN interactions in the crystal

Metal	Occupancy	Interacting residues[a]	Coordination geometry[b]	*B*-factor (metal)	*B*-factor (surrounding atoms)[b]
Co1	1.00	His44(A)	–	61.9	39.0
Co2	0.57	–	–	19.8	21.0
Co3	0.36	Asp102(B), Asp31(B)	Octahedral	20.4	27.2
Co4	0.57	Asp31(B)	Octahedral	17.4	23.7
Co5	0.24	Glu5(A)	–	20.7	35.2
Co6	0.31	–	–	31.5	33.4
Eu1A	0.59	Asp102(B), Thr104(B)	Octahedral	41.0	49.5
Eu1B	0.41	Asp102(B)	–	36.0	39.5
Eu2A	0.54	Glu22(A)	Square planar	36.2	35.8
Eu2B	0.46	–	Square planar	36.4	29.0
Eu3	0.71	Asp29(B), Asp31(B)	Octahedral	48.7	41.8
Eu4	0.43	Glu22(B)	Trigonal bipyramid	27.7	50.8
Eu5A	0.47	Asp29(A)	–	41.4	34.4
Eu5B	0.53	Asp29(A)	–	62.8	37.2
Eu6	0.28	Gln52(B)	–	35.8	39.9
Eu7A	0.50	Glu42(B)	–	70.8	57.4
Eu7B	0.50	Asp27(B)	Square planar	90.9	52.8
Eu8A	0.50	Gln32(A)	Octahedral	66.7	47.9
Eu8B	0.50	–	–	71.9	50.6
Eu9	0.40	Glu5(A)	–	79.2	51.0

[a] Residues within a distance of 3.0 Å from the indicated metal. The corresponding chain is indicated in parentheses

[b] Idealized geometry assignment and valence-weighted environmental average *B*-factor were calculated using the CheckMyMetal web server [47]

ligand binding to pre-formed apo-crystals must be compatible with crystal packing [35], and in the case of soaking experiments using charged ligands, local electrostatics in the crystal lattice may also influence site occupancy. For these reasons, the two molecules in the asymmetric unit provide complementary views of metal binding to pFXN, as discussed below.

The pFXN structures reveal multiple protein–metal contacts disseminated throughout the structure, but near a half of metal-interacting residues are located in the acidic ridge (Figs. 3, 4 and S3). The acidic character of these residues, and even the identity of some of them, is evolutionary conserved, and NMR-monitored titrations of transition metals interactions with the homolog eFXN reveal the metal-binding ability of this acidic patch in solution [10, 18]. This evidence supports an important functional role for the observed metal interactions within the acidic ridge also for pFXN. The residues and metal ions interacting through this region include Glu22 and Glu23 binding to Eu2, Eu4 or Co6 (depending on protein chain and metal derivative); Asp27 interacting with Eu7; Asp29 coordination with Eu3 or Eu5; and Asp31 interacting with Eu3, Eu8, Co3 and Co4. The non-conserved residue Asp42 participates in coordination of Eu7 along with Asp27 and it is also perturbed during titrations of eFXN with metals [18].

Most of the protein–metal interactions observed are sequentially local, or involve the coordination by a single side-chain (Figs. 3, 5a). However, there are two cases where binding occurs through residues distant in sequence (Fig. 5b), through the concurrence of side-chains from different secondary structure elements. The first case involves the above-mentioned coordination of Eu7 by Asp27 and Asp42. The second case involves the coordination of Co2 by four atoms of pFXN backbone: the amide group and carbonyl oxygen of Trp76, and the amide groups of Phe85 and Leu86. In addition, two water molecules complete the coordination. Even though sequence conservation of Trp76 and Phe85 is high, and the atypical structural features of this site with a partially buried metal are suggestive, the distances between metal and protein are larger than 3.3 Å (Fig. 5b), too large for a tight coordination. Then, we hypothesize this metal-binding site might be not relevant for function.

Some of the observed metal interactions are similar to those found in eFXN structures [18], sharing at least one conserved amino acid residue per interacting site (Figure S3). This is the case of some of the above-mentioned binding sites at the acidic ridge, involving the metal ions Eu3, Eu5, Eu7, and Eu8, and residues Asp27, Asp29, and Asp31 of loop1. In addition, one binding site is located at the

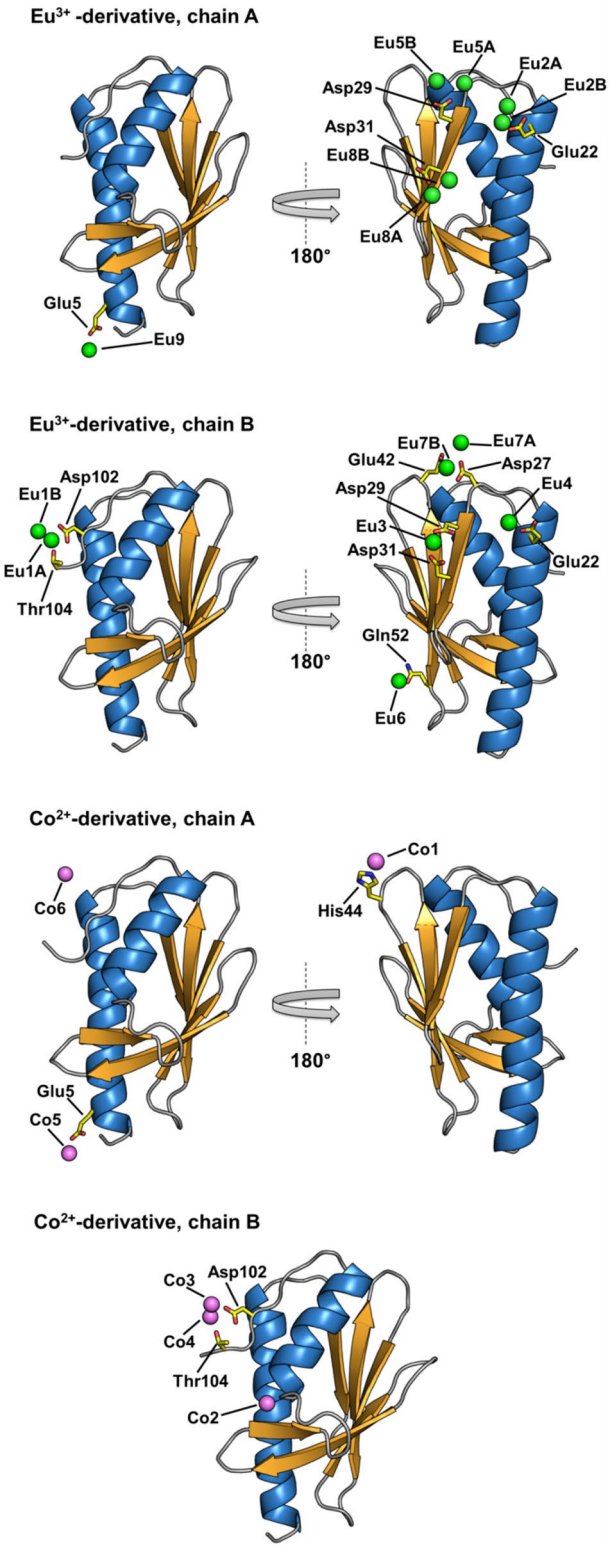

Fig. 3 Localization of metal ions associated with pFXN structures. Metal ions are represented as *spheres* of 1 Å radius, along with the side-chains involved in metal coordination (using a distance cutoff of 3 Å). Protein chains are shown as *ribbon models*. For clarity, each chain is rotated by 180° along the indicated axis, and the total amount of metal ions is shown split into *two images*

N-terminus of helix α1 for both homologs: Eu9 and Co5 interact with the Glu5 side-chain in the pFXN, whereas Asp3 is the interacting residue in the case of eFXN. The Glu5 is a semi-conserved residue in the FXN family, however, this residue is not perturbed in the metal titrations of eFXN [18], therefore, the functional relevance of this interaction is speculative at present.

There are two metal-binding sites shared by Co^{2+} and Eu^{3+} derivatives. The first one involves the Glu5 interaction described in the previous paragraph. The second case is located at the C-terminus, and involves Asp102 and Thr104 from chain B interacting with Eu1 or Co3/Co4 (Fig. 6). The C-terminal of FXN family is a highly variable region, and accordingly residues 102 and 104 lack of sequence conservation, suggesting this metal-binding site is not important for function. However, this interaction may be implicated in flexibility modulation of some other regions of the molecule, as explained in the "Discussion". In addition to Asp102 and Thr104, Co3 is also coordinated via inter-subunit interaction with Asp31 of a symmetry-related molecule. Remarkably, this contact is absent in the Eu^{3+} derivative, more likely due to the rotation of the Asp31 side-chain that allows intramolecular coordination of Eu3 with participation of Asp29, suggesting some degree of preference for Eu^{3+} at this site. Given the predominantly monomeric nature of pFXN at low concentrations, and the proposed model for interaction with the Fe–S cluster biosynthetic complex, where one FXN molecule interacts with each chain of the IscS dimer [36], this intermolecular interaction is probably a crystal packing artifact devoid of functional relevance.

There are two other metal interactions far from the acidic ridge: a highly conserved Gln52 interacts with Eu6 of chain B, and the non-conserved His44 interacts with Co1 in chain A. The functional relevance of these sites is not clear and merits further research.

The effects of metal binding on the pFXN structure

Metal binding does not induce major structural rearrangements either in Co^{+2} or Eu^{+3} derivatives, as reflected by the average pairwise RMSD for backbone atoms between apo and metal-bound derivatives (0.40 ± 0.08 Å) (Fig. 7). Only a slight shift in the positions of backbone atoms is observed for loop5 in both Co^{+2} and Eu^{+3} derivative structures. The acidic residues involved in metal binding do not experience rotamer changes upon binding, except for residues Asp29 and Asp31 of chain B in the Eu^{+3} derivative (Fig. 8). This evidence suggests that most of the metal-binding sites in pFXN are essentially already formed in apo-pFXN.

As subtle alterations in protein dynamics may take place upon binding, we evaluated changes in motions through the analysis of crystallographic *B*-factors. Because

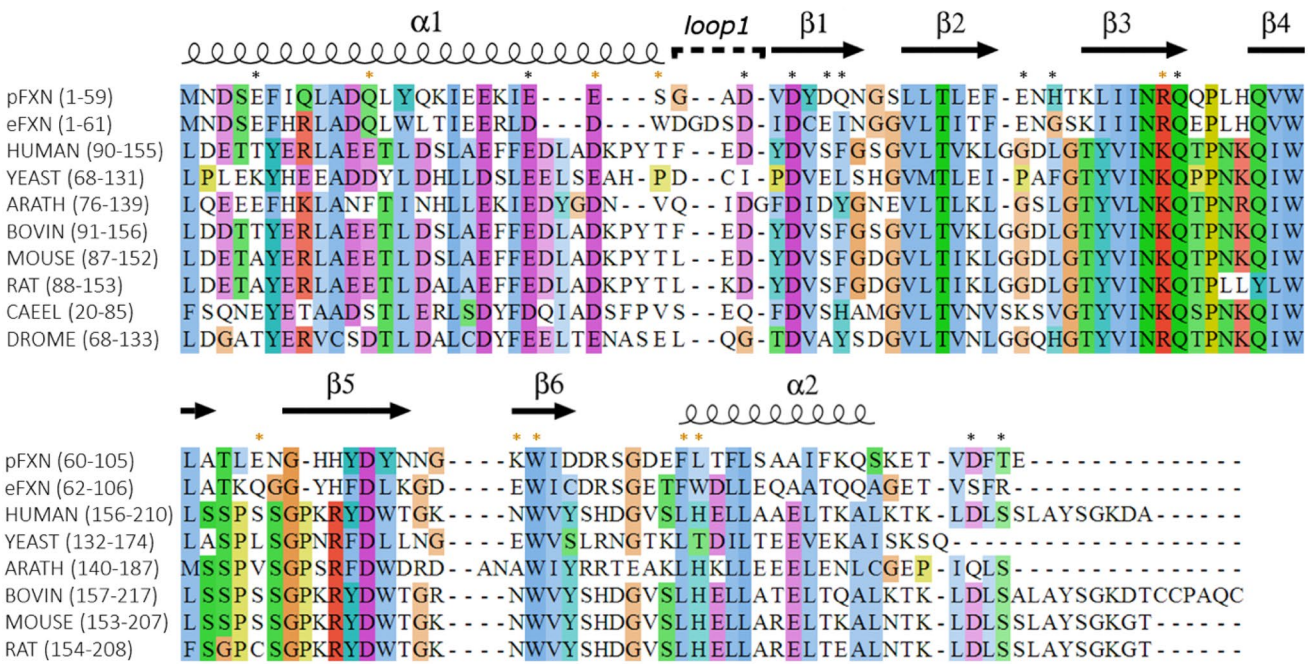

Fig. 4 Multiple sequence alignment of FXN variants. pFXN residues that exhibit metal ions located in their vicinity are marked with *asterisk*: those at distance ≤3 Å are shown in *black* whereas *orange* is used for distances between 3 and 4 Å. The FXN sequences come from *Psychromonas ingrahamii* (pFXN), *Escherichia coli* (eFXN), *Homo sapiens* (HUMAN), *Saccharomyces cerevisiae* (YEAST), *Arabidopsis thaliana* (ARATH), *Bos taurus* (BOVIN), *Mus musculus* (MOUSE), *Rattus norvegicus* (RAT), *Caenorhabditis elegans* (CAEEL) and *Drosophila melanogaster* (DROME). Sequences were colored according to the ClustalX convention to highlight conservation features of each residue. The intensity of shading increases according to conservation

inaccuracies in model binding may conduct to artifactual *B*-factors, we performed a comprehensive analysis of model quality, using metrics derived from electron density maps [31]. The real-space *Z*-scores (RSZD) are metrics of the local model accuracy, computed using the difference Fourier map, a commonly used map during structure solution to check for errors in atom's placing. Particularly, the RSZD− score accounts for misplaced atoms (because it reflects the lack of observed density compared with predicted from the model), whereas RSZD+ accounts for unexplained density or missing atoms. In addition, the RSZO scores the model precision, because it accounts for the ratio of average observed electron density to the signal-to-noise ratio in a specified region. We did not detect significant higher RSZD+ or RSZD− values in none of the pFXN structures (Figures S4 and S5), indicating no significant inaccuracies in the models (coordinates, occupancies and *B*-factors), therefore, the *B*-factors are reliable indicators of the protein dynamics. Simultaneously, we investigated the influence of crystal packing in *B*-factors by considering the change in intermolecular contacts in a radial distribution around each amino acid residue. Packing is mostly similar between metal derivatives and apo-pFXN (Fig. 7), with a few significant differences in residues located at loops β1–β2 and β4–β5, and the last portion of helix α2. There are two stretches that exhibit the largest changes in *B*-factors (Fig. 7). The first one corresponds to an increase of values for residues near position 81 of chains A in both derivatives. No metal is observed in the immediate region surrounding this segment for either structure, and the change occurs without significant packing alterations in the Co derivative, with only a small decrease in packing of the Eu derivative. Interestingly, a positively charged residue is evolutionary conserved in position 80 (corresponding to Arg in pFXN, Figure S6). The second stretch exhibits a decrease in *B*-factors in both derivatives, and involves residues near position 63 for chains B. The latter is coincident with a packing reduction for the two derivatives and the largest change in RMSD between the metal bound and apo-pFXN. Additionally, this region exhibits the highest *B*-factor values in the crystal structures and it is predicted as a locally unstable region by the COREX–BEST algorithm [11]. Whereas the *B*-factor difference occurs in both derivative structures, protein–metal interaction is detected within this region in only one of these, corresponding to Eu8A at 3.97 Å distance from the main chain oxygen of Glu64. This fact suggests that the reduction of internal mobility in this stretch is not due to the sole presence of a metal ion or due

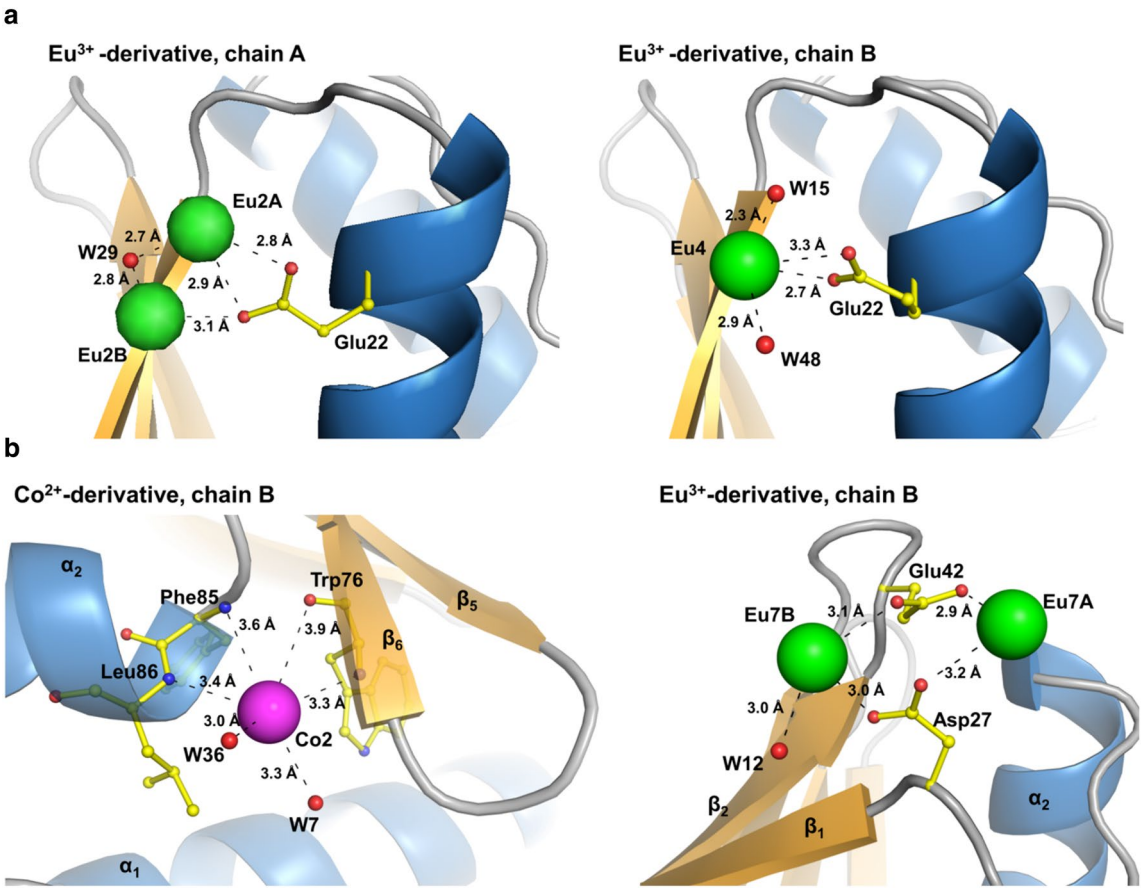

Fig. 5 Close-up views of sequentially local and non-local binding sites of pFXN. **a** Local sites: *left* and *right panels* are ribbon representations of pFXN showing the interaction of Eu^{3+} with Glu22 from chain A or B chain, respectively. **b** Non-local sites: Co2 interacts with backbone atoms of Trp76 (strand β6), Phe85, and Leu86 (helix α2), whereas Eu7 interacts with the side-chains of Asp27 (loop1) and Glu42 (loop3). Water molecules (identified by *W*) involved in metal coordination are shown as *small red spheres*. The interatomic distances are indicated by *dashed lines*

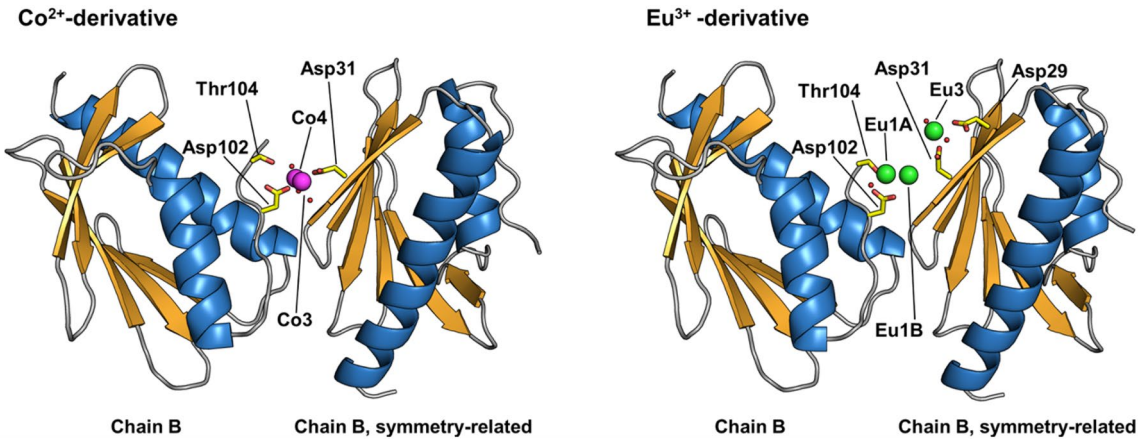

Fig. 6 Detailed view of a metal-binding site present in both Co^{2+} and Eu^{3+} derivatives of pFXN. The chain B of pFXN, and the same chain from a symmetry-related molecule are shown as ribbon models. Side-chains of residues involved in coordination are represented as sticks, whereas metal ions are drawn as *spheres* of 1 Å radius, with associated water molecules shown as *smaller red spheres*

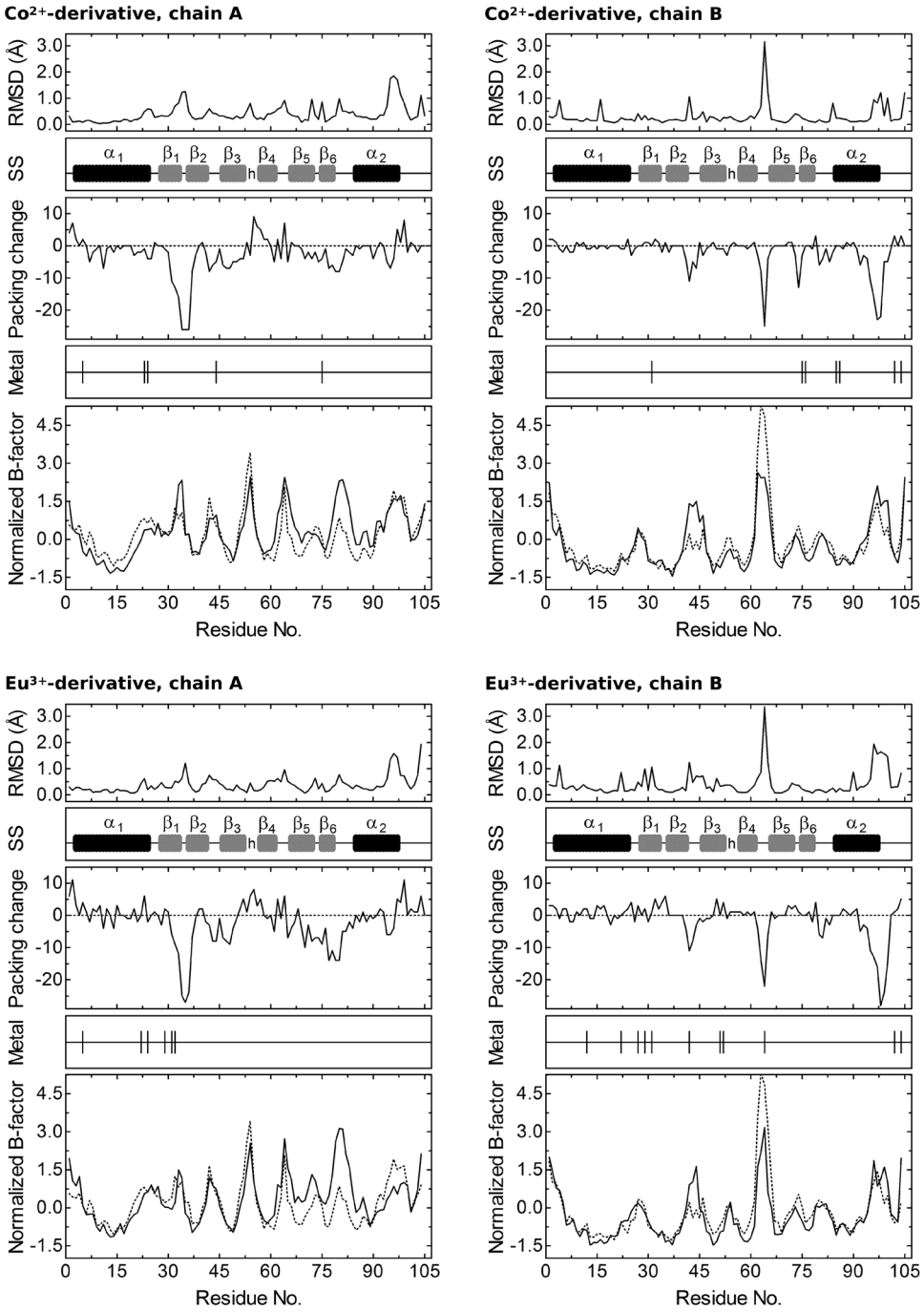

Fig. 7 Changes in pFXN crystal structures resulting from Co^{2+} and Eu^{3+} additions. In the *upper panel*, the RMSD between the metal-containing chain and the corresponding one from the apo form are shown. Intermolecular packing was evaluated as the number of atoms of symmetry or NCS-related chains within a 10 Å sphere centered at each alpha carbon, and the difference between metal derivative and apo-pFXN is shown in the *middle panel*. Normalized *B*-factors of derivatives (*solid line*) and apo-pFXN (*dotted line*), averaged over main chain atoms in each residue, are shown in the lower panel. Residues located within a distance of 4.0 Å from the metal ion are indicated by *vertical bars*, and the secondary structure (*SS*) is also indicated

to the change in local packing (because the latter is a consequence of a reduction in intermolecular contacts); rather, metal binding may be coupled with a slight conformational change in this region, thus having an impact on conformational flexibility.

In vitro iron-binding activity of pFXN

To obtain some indication about iron-binding affinity by pFXN, we carried out binding experiments monitored by fluorescence quenching of tryptophan residues. These experiments take advantage of the fact that binding of ferric ion clearly reduces the intrinsic protein fluorescence of pFXN (Fig. 9a, b), as result of Förster energy transfer (FRET) from tryptophan to absorption bands generated by iron binding to the protein [37–39]. To circumvent iron precipitation, which is enhanced at neutral pH, we performed the experiments at pH 4.8, the same pH used in crystallization, in 20 mM sodium acetate, 100 mM NaCl buffer. It should be noted that, even this pH is near to the pI of the

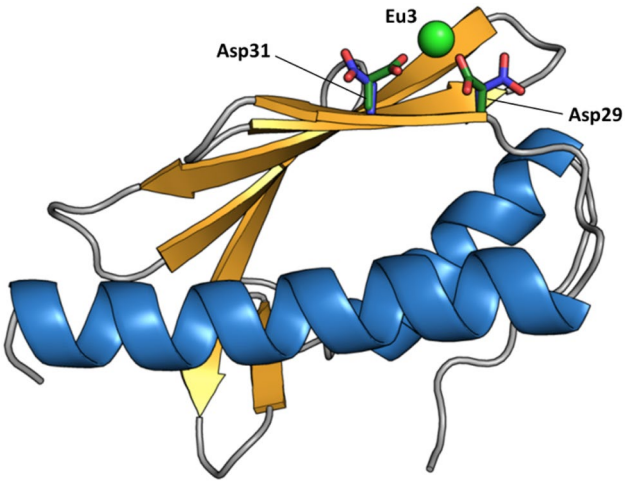

Fig. 8 Acidic residues exhibiting rotamer changes upon binding. The side-chains of Asp29 and Asp31 of chain B in the Eu^{3+} derivative (*green*), and the same side-chains of apo-pFXN (*blue*) are shown. The metal is represented as a *sphere* of 1 Å radius

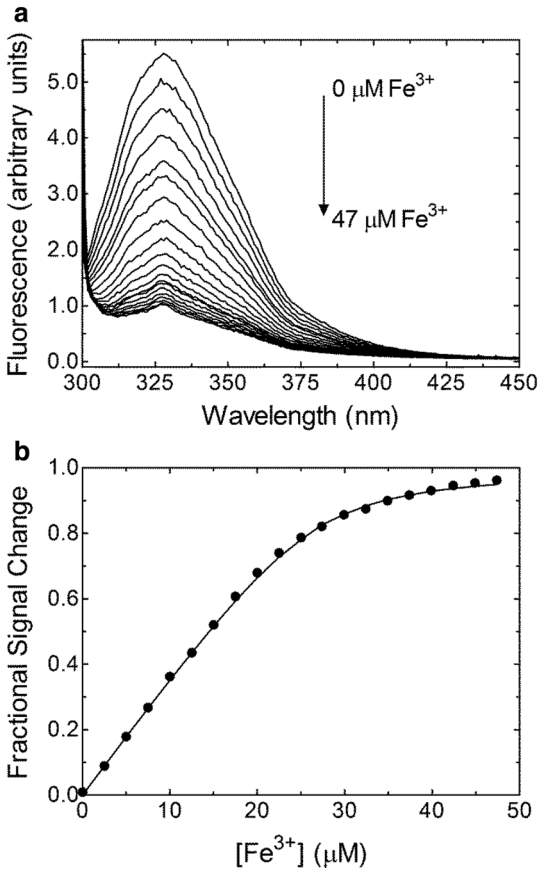

Fig. 9 In vitro iron binding by pFXN. **a** Binding of Fe^{3+} followed by the quenching of Trp fluorescence. The experiment was performed in a 20 mM sodium acetate buffer pH 4.8, 100 mM NaCl. **b** Fitting of the binding model described in the "Materials and methods" (*solid line*) to the fluorescence data. The *circles* represent the average of three independent experiments, and the values of fitted parameters and derived standard deviations are given in the text

protein (which is 4.39), pFXN is monomeric at concentrations used for the experiments (Figure S2). The same results were obtained when experiments were repeated with the protein sample stored for up to 4 days in this condition at 4 °C (data not shown). Thus, interference of dimer or higher order oligomers in the iron titrations is discarded. These experiments allowed us to obtain highly reproducible values of K_D for Fe^{3+} ($1.2 \pm 0.3\ 10^{-6}$ M) and stoichiometry ($p = 4.4 \pm 0.2$). These results show that at least 4 iron atoms bind to the surface of pFXN in the vicinity of the Trp residues, close enough to produce the quenching of Trp.

Discussion

In this work, we solved the crystal structures of a cold-adapted frataxin from *Psychromonas ingrahamii* in the presence of cobalt or europium ions. We identified a number of metal-binding sites, mainly solvent exposed, and several of them are novel sites when compared with previous studies on the mesophilic homolog from *E. coli*. Two protein molecules were found in the asymmetric unit. It remains unknown whether or not there is any biological relevance to the moderate tendency to dimerize in solution and the inter-subunit interactions observed in the crystal structures of pFXN. A biologically relevant dimer might enhance the iron-binding capability of pFXN through the interaction of metal ions with the surface formed by dimerization, in analogous way to the observed for eFXN, which is able to bind more than twenty iron atoms per monomer when it aggregates [15]. In this context, we have not detected oligomerization upon addition of iron to pFXN using native gel electrophoresis (Figure S7), indicating that iron-induced pFXN oligomerization is not likely to occur. Similarly, for mature human FXN it was confirmed that the monomer is the functional species [40, 41]. On the other hand, the existence of an iron-induced aggregation process yielding a high molecular weight oligomer with enhanced capability for iron binding has already been described for yeast FXN [42]. In the latter case, an extra N-terminal segment, absent in both pFXN and its mesophilic counterpart eFXN, has proven to be a critical element for oligomerization [43].

The evidence presented here suggests that most of the side-chain involved in metal binding in pFXN do not experience rotameric changes upon binding. We reasoned that in the case of pFXN, pre-organized ligand-binding sites could reduce the penalties in configurational and solvation entropies associated, respectively, with the loss of degrees of freedom and solvent reorganization (for both the ligand and the

binding site) that occur upon binding as described for other systems [44]. However, in a broad context, side-chain conformational rearrangements are common in protein structures upon metal binding, a study by Babor and coworkers shows that nearly 40 % of the metal-binding sites studied display side-chains undergoing conformational change, when the apo and holo structures are compared [45].

The observed affinity of pFXN for Fe^{3+} resembles previous results obtained for the homolog eFXN, in which Fe^{2+} binds to the protein with a $K_D = 4$ μM and $p = 2$ [15]. Remarkably, Fe^{3+} ($p = 6$) and Fe^{2+} ($p = 6$–7) bind to the human FXN homolog with K_D of 12 and 55 μM, respectively [46]. These results as a whole indicate the existence of heterogeneity in the iron-binding mode through the FXN protein family.

Although pFXN has evolved in the context of a psychrophilic organism, where protein flexibility is expected to be enhanced for a proper function at low temperatures, no major rearrangements in the structure were observed upon metal binding. Nevertheless, binding of metal ions to the protein surface resulted in a significant decrease in the *B*-factor values of the highest mobile region in pFXN (residues 59–68). Independently of which metal ion is bound (Co^{2+} or Eu^{3+}) to pFXN, we have observed similar changes in *B*-factors when the same chain in both derivatives is compared. Because we have detected shared binding regions between both derivatives, we propose that those binding sites could act modulating the flexibility of the regions with largest changes in *B*-factors. Specifically, the shared binding region in chain A comprises the first portion of helix-1 (including Glu5) and the last residues of the same helix (Glu22/Glu23). For chain B, the equivalent binding region is located at the C-terminal of the protein (including residues Asp102 and Thr104). However, we cannot rule out whether changes in the global electrostatics in the context of the crystal assembly modulate the flexibility of the regions with the largest changes in *B*-factors.

It has been reported that cysteine desulfurase interacts with the acidic ridge of frataxin through a positive patch in the context of the Fe–S cluster assembly machinery [36], highlighting the importance of electrostatic interactions for frataxin function. NMR experiments in the homologous eFXN reported that the region involving residues 59–68 was significantly affected by the addition of the scaffolding protein IscU, a member of the Fe–S cluster biosynthetic complex, suggesting a direct contact between partner proteins mediated by this region [36]. Consequently, we speculate that metal binding at shared binding regions could regulate pFXN interactions with partner proteins.

In summary, the crystallographic study of pFXN allowed us a detailed characterization of metal–protein interactions. As expected, metal-binding sites are mainly located in the acidic region, but there are other sites spread over the protein surface. In this context, we suggest that solvent-exposed metal-binding sites of moderated affinities found in pFXN allow metal exchanges through a quick capture and release of iron to partner proteins. The structural evidence provided in this work should assist in the design of new experiments to test the biological relevance of the metal-binding sites found in the frataxin family of proteins.

Acknowledgments This work was supported by the Agencia Nacional de Promoción Científica y Tecnológica (ANPCyT), the Consejo Nacional de Investigaciones Científicas y Técnicas (CONICET), Universidad de Buenos Aires (UBACyT), the CNRS, the INSERM, the Université de Strasbourg, the Région Alsace, the Hôpital Civil de Strasbourg, Instruct [part of the European Strategy Forum of Research Infrastructures (ESFRI)] and the French Infrastructure for Integrated Structural Biology (FRISBI) ANR-10-INSB-05-01. We specially thank the IGBMC Structural Genomics Platform staff (in particular, Pierre Poussin Courmontagne and Dr. Alastair McEwen). The crystallographic experiments were performed on the X06DA beamline at the Swiss Light Source, Paul Scherrer Institut, Villigen, Switzerland. In particular, we thank Christian Stirnimann and Vincent Olieric for their help on the beamline.

References

1. Musco G, Stier G, Kolmerer B, Adinolfi S, Martin S, Frenkiel T, Gibson T, Pastore A (2000) Structure 8:695–707
2. Pastore A, Puccio H (2013) J Neurochem 126(Suppl 1):43–52
3. Bridwell-Rabb J, Iannuzzi C, Pastore A, Barondeau DP (2012) Biochemistry 51:2506–2514
4. Lu C, Cortopassi G (2007) Arch Biochem Biophys 457:111–122
5. Li DS, Ohshima K, Jiralerspong S, Bojanowski MW, Pandolfo M (1999) FEBS Lett 456:13–16
6. Dhe-Paganon S, Shigeta R, Chi YI, Ristow M, Shoelson SE (2000) J Biol Chem 275:30753–30756
7. He Y, Alam SL, Proteasa SV, Zhang Y, Lesuisse E, Dancis A, Stemmler TL (2004) Biochemistry 43:16254–16262
8. Karlberg T, Schagerlof U, Gakh O, Park S, Ryde U, Lindahl M, Leath K, Garman E, Isaya G, Al-Karadaghi S (2006) Structure 14:1535–1546
9. Cho SJ, Lee MG, Yang JK, Lee JY, Song HK, Suh SW (2000) Proc Natl Acad Sci USA 97:8932–8937
10. Nair M, Adinolfi S, Pastore C, Kelly G, Temussi P, Pastore A (2004) Structure 12:2037–2048
11. Roman EA, Faraj SE, Cousido-Siah A, Mitschler A, Podjarny A, Santos J (2013) Biochim Biophys Acta 1834:1168–1180
12. Foury F, Pastore A, Trincal M (2007) EMBO Rep 8:194–199
13. Aloria K, Schilke B, Andrew A, Craig EA (2004) EMBO Rep 5:1096–1101
14. Correia AR, Wang T, Craig EA, Gomes CM (2010) Biochem J 426:197–203
15. Bou-Abdallah F, Adinolfi S, Pastore A, Laue TM, Dennis Chasteen N (2004) J Mol Biol 341:605–615
16. Yan R, Konarev PV, Iannuzzi C, Adinolfi S, Roche B, Kelly G, Simon L, Martin SR, Py B, Barras F, Svergun DI, Pastore A (2013) J Biol Chem 288:24777–24787
17. Riley M, Staley JT, Danchin A, Wang TZ, Brettin TS, Hauser LJ, Land ML, Thompson LS (2008) BMC Genom 9:210
18. Pastore C, Franzese M, Sica F, Temussi P, Pastore A (2007) FEBS J 274:4199–4210
19. Correia AR, Adinolfi S, Pastore A, Gomes CM (2006) Biochem J 398:605–611

20. Adinolfi S, Nair M, Politou A, Bayer E, Martin S, Temussi P, Pastore A (2004) Biochemistry 43:6511–6518
21. Roman EA, Faraj SE, Gallo M, Salvay AG, Ferreiro DU, Santos J (2012) PLoS ONE 7:e45743
22. Otwinowski Z, Minor W (1997) Methods Enzymol 276:307–326
23. Brunger AT (1992) Nature 355:472–475
24. McCoy AJ, Grosse-Kunstleve RW, Adams PD, Winn MD, Storoni LC, Read RJ (2007) J Appl Crystallogr 40:658–674
25. Adams PD, Afonine PV, Bunkoczi G, Chen VB, Davis IW, Echols N, Headd JJ, Hung LW, Kapral GJ, Grosse-Kunstleve RW, McCoy AJ, Moriarty NW, Oeffner R, Read RJ, Richardson DC, Richardson JS, Terwilliger TC, Zwart PH (2010) Acta Crystallogr D Biol Crystallogr 66:213–221
26. Keegan RM, Winn MD (2008) Acta Crystallogr D Biol Crystallogr 64:119–124
27. Winn MD, Ballard CC, Cowtan KD, Dodson EJ, Emsley P, Evans PR, Keegan RM, Krissinel EB, Leslie AG, McCoy A, McNicholas SJ, Murshudov GN, Pannu NS, Potterton EA, Powell HR, Read RJ, Vagin A, Wilson KS (2011) Acta Crystallogr D Biol Crystallogr 67:235–242
28. Murshudov GN, Skubak P, Lebedev AA, Pannu NS, Steiner RA, Nicholls RA, Winn MD, Long F, Vagin AA (2011) Acta Crystallogr D Biol Crystallogr 67:355–367
29. Emsley P, Cowtan K (2004) Acta Crystallogr D Biol Crystallogr 60:2126–2132
30. Chen VB, Arendall WB 3rd, Headd JJ, Keedy DA, Immormino RM, Kapral GJ, Murray LW, Richardson JS, Richardson DC (2010) Acta Crystallogr D Biol Crystallogr 66:12–21
31. Tickle IJ (2012) Acta Crystallogr D Biol Crystallogr 68:454–467
32. van de Weert M (2010) J Fluoresc 20:625–629
33. Sawyer WH, Winzor DJ (2001) Curr Protoc Protein Sci 16:5A:A.5A.1–A.5A.40
34. Krissinel E, Henrick K (2007) J Mol Biol 372:774–797
35. Danley DE (2006) Acta Crystallogr D Biol Crystallogr 62:569–575
36. Prischi F, Konarev PV, Iannuzzi C, Pastore C, Adinolfi S, Martin SR, Svergun DI, Pastore A (2010) Nat Commun 1:95
37. Lehrer SS (1969) J Biol Chem 244:3613–3617
38. James NG, Ross JA, Mason AB, Jameson DM (2010) Protein Sci 19:99–110
39. Dunning Hotopp JC, Auchtung TA, Hogan DA, Hausinger RP (2003) J Inorg Biochem 93:66–70
40. Schmucker S, Argentini M, Carelle-Calmels N, Martelli A, Puccio H (2008) Hum Mol Genet 17:3521–3531
41. Bencze KZ, Kondapalli KC, Cook JD, McMahon S, Millan-Pacheco C, Pastor N, Stemmler TL (2006) Crit Rev Biochem Mol Biol 41:269–291
42. Adamec J, Rusnak F, Owen WG, Naylor S, Benson LM, Gacy AM, Isaya G (2000) Am J Hum Genet 67:549–562
43. Soderberg CA, Shkumatov AV, Rajan S, Gakh O, Svergun DI, Isaya G, Al-Karadaghi S (2011) J Mol Biol 414:783–797
44. Singh N, Warshel A (2010) Proteins 78:1724–1735
45. Babor M, Greenblatt HM, Edelman M, Sobolev V (2005) Proteins 59:221–230
46. Yoon T, Cowan JA (2003) J Am Chem Soc 125:6078–6084
47. Zheng H, Chordia MD, Cooper DR, Chruszcz M, Muller P, Sheldrick GM, Minor W (2014) Nat Protoc 9:156–170